CHAPTER 4

Synthesis and Characterization of CeO_2 and $MgSiO_3$ materials, sensor fabrication and measuring unit

Contents

4.1 Introduction

This chapter explains the synthesis/preparation and characterization of CeO2 NPs and magnesium silicate ($MgSiO_3$) materials for the development of capacitive sensors based on IDE structures which was designed and simulated in chapter 3. The CeO_2 NPs based sensor has been used for bitterness assessment in citrus fruit juices through the detection of the phytochemical limonin whereas the sensor developed using magnesium silicate as sensor material detects limonin in citrus fruit juices and also measures the reduction of limonin content through selective adsorption of it on the surface of magnesium silicate. The sensor fabrication and measurement set-up based on the charging–discharging of the capacitive sensor is also explained in this chapter.

Cerium belonging to the rare earth lanthanide series has two oxidation states (+3 and +4)[1]. The oxide of Cerium (CeO_2) represents the cubic fluorite structure with oxygen deficiencies, providing redox reaction sites [2]. The NPs with their excellent properties such as miniature size and shape and high surface-to-volume ratio have drawn much attraction in industrial, environmental and medical applications [3, 4]. Likewise, CeO_2 NPs have also a wide range of applications such as catalysts [5, 6], sensors, sunscreen cosmetics, fuel cells with solid oxide, chemicals alteration in the body, antibacterial activity, drug delivery carriers, anti-parasitic ointments, therapeutics agents, etc [7-9]. Compared to other metal oxide NPs such as TiO_2 and ZnO, CeO_2 NPs possess less toxicity when applied to cell activity [10]. The NPs are efficient in the degradation of pollutants from wastewater [11]. Recently CeO_2 NPs have been tested for antibacterial behaviour using gram-positive and gram-negative bacteria [12]. The CeO_2 NPs with anti-oxidant activity have potential applications in daily human life as evaluated by various researchers [13, 14].

There are many methods reported for the synthesis of NPs –microwave [15][15], hydrothermal [16], flame spray pyrolysis [17], sonochemical [18], sol-gel, and co-precipitation methods [19]. Although these physical and chemical methods control the size and shape of NPs, these methods use toxic materials that also require high temperature and pressure, and lesser biocompatibility [2, 9, 20, 21]. The green synthesis methodologies in the synthesis of metal and metal oxide NPs offer advantages such as large-scale commercial production and pharmaceutical applications, etc. Furthermore, green synthesis of nanostructures especially metal oxide nanoparticles has emerged as a simple, non-toxic, inexpensive and efficient approach for nanofabrication. In this

direction, biosynthesis of inorganic nanostructures such as oxide nanoparticles, sulphide nanoparticles, metallic nanoparticles and other nanostructures have been reported for a wide range of applications such as drug delivery, antibacterial activity, gene therapy, DNA analysis, bio-sensing, magnetic resonance fingerprinting (MRF) imaging extract [22]. The plant extracts, micro-organisms and biological products are used for the biosynthesis of nanostructures especially metallic nanoparticles where phenolic groups, polyphenols and terpenoids reduce particle size making nanostructure forms [23]. Moreover, biosynthesis provides stabilities and bioavailability of NPs [24].

The biosynthesis of CeO_2 NPs is carried out by using plant extracts such as Acalypha indica [25], Petroselinum crispum [26], Gloriosa superba [7]. The fungal extracellular compound Humicola sp. is also used for the synthesis of CeO_2 NPs [27]. Here, the plant extract stabilizes the NPs and acts as a capping agent [24] but fabricates NPs of large size. Apart from the plant extract, honey, egg white, pectine are also used for isotropic growth of nutrient-mediated biosynthesis of CeO_2 NPs [28]. Dillenia indica (D. indica) fruits consisting of phenolic groups have already been reported for the reduction of metallic oxides for making nanostructure [29]. Here, the green synthesis of CeO_2 NPs using D. indica aqueous extract has been presented for the first time. The formation of CeO_2 NPs was characterized by physicochemical investigation such as XRD analysis, EDX spectra and FTIR spectra.

So far of our awareness, no work has been reported for the detection as well as reduction of limonin measurement using the same device. Here an attempt has been made for the same using magnesium silicate as a sensor material. Charles R. Barmore et al. [30] reported a reduction in bitterness and tartness in citrus juice by exposing the juice to magnesium silicate in batches with its different concentrations (w/v) for 1 min duration at 20 ℃. $MgSiO_3$ exhibited the highest reduction of limonin by 81% in grapefruit juice in comparison to other ingredients like naringin(51%), narirutin(57%) and total acid contents(59%) [30, 31]. Hence, the magnesium silicate material has been prepared, activated and characterized for use as a sensor material.

The chapter also describes the fabrication steps involved in the development of low-cost sensors made on the paper substrate over the IDE structure. Quantification of limonin content in citrus fruit juices needs an accurate, portable measuring set-up to make it suitable for onsite measurement. In an aim to reach this objective, a portable measuring setup has been developed instead of using a bulky as well as costly impedance analyzer. Measurement setup for capacitance of the sensor has been explained in this chapter

4.2. Materials and Methodology

4.2.1 Materials

The raw chemicals and reagents of analytical grade were used in the synthesis process without any further purification. Ammonium Cerium (IV) Nitrate [$Ce(NH_4)_2(NO_3)_6$] was procured from Alfa Aesar company, India. Dillenia indica fruits were obtained from the tree locally available at Tezpur University, Assam, India. Standard Limonin powder was procured from Sigma Aldrich. The other chemicals such as citric acid, ascorbic acid, and sugars of analytical grade were procured from Alfa Aesar company. The polyvinyl alcohol (PVA) powder, Magnesium silicate ($MgSiO_3.xH_2O$), were purchased from Alfa Aesar company, India. India. For solvent and other applications, deionized (DI) water was utilized. The raw chemicals were of analytical graded and used without further purification

4.2.2 Synthesis of CeO_2 NPs

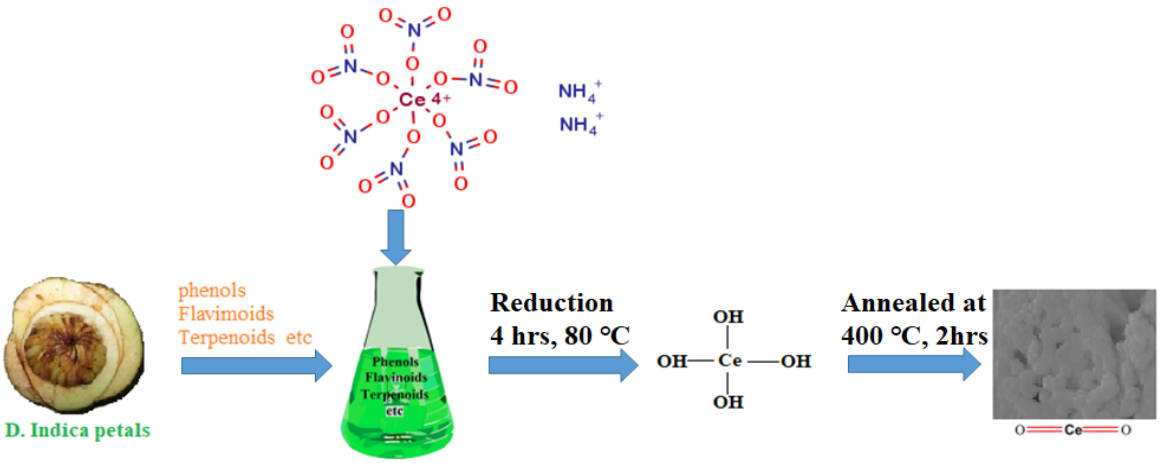

Figure.4.1: steps for green synthesis of CeO_2 nanoparticles using D. indica petal aqueous extract

The D. indica fruits were first cleaned using running water and small pieces were made thereafter. The seeds were removed from the pieces and 40 g of the petals from the fruit were soaked in 100 mL of DI water. The mixture was then stirred at a temperature of 80 ℃ for 1 h. Using muslin cloth the suspension was filtered and the filtrate was centrifuged at 5000 rpm for 15 mins. The clear supernatant was collected after centrifuging and used as the extract during the reduction process. In the green synthesis

process as shown in Fig. 4.1, 0.4 g of $Ce(NH_4)_2(NO_3)_6$ was added with 200 ml of DI water and stirred well until a clear solution was achieved. The 40 ml of D. indica petal extract was added to the above solution which was then kept in a reflux condenser (Fig 4.2). The mixture was continued to heat (80 ℃) in reflux condition with constant stirring (400 rpm) for 4 h. The resultant was then filtered and washed with DI water repeatedly to remove impurities. The washed sample was then dried in a vacuum oven for 8 h at 60 ℃ to obtain as-synthesized CeO_2 NPs sample (C1). The powder sample of CeO_2 NPs annealed at 300 ℃, 400 ℃ and 500 ℃ are denoted as C2, C3 and C4 respectively.

Figure 4.2: Reflux condenser

4.2.3 Characterization of synthesized of CeO_2 NPs

FTIR analysis of cerium oxide nanoparticles (CNP) was done in the region of 400- 4000 cm^{-1} using NICOLET, IMPACT 410 OMNIC E.S.P.5.0 spectrometer to study the surface functional groups of as-prepared and annealed samples. The powder X-ray diffraction (XRD) pattern was obtained by using a BRUKER D8 Focus diffractometer and from the XRD pattern, the crystal size was determined. The UV-vis spectroscopy was used for the quantitative determination of NPs. Field emission scanning electron microscopy (FESEM) (JEOL, model JSM 7200 F, Japan) and Transmission Electron Microscope (TEM),(JEOL, Model: JEM 2100) were employed to examine surface morphology, and the elemental composition of materials was estimated by Energy Dispersive X-Ray Analysis (EDX).

The broadband, 3200 - 3700 cm^{-1} of the FTIR spectrum of as-synthesized CeO_2 NPs (C1) in Fig. 4.3a indicates the stretching of hydroxyl groups [32, 33]. The reduction in the depth of transmittance peaks at 3700 cm^{-1} after annealing showing the reduction of OH^{-1} ions. As the annealing temperature increases, the depth of transmission peaks decreases and gets almost saturated at 400 ^{0}C indicating very less reduction of OH^{-1} after 400 ^{0}C. The bands for the C1, C2, C3, and C4 samples at 1628, 1630, 1642, and 1562cm^{-1} represent H-O-H bending since the water was absorbed on the sample's surface and partially overlapped with the O-C-O stretching band [7]. The depth of the transmittance

spectrum at 1630–1642 cm^{-1} reduces due to a decrease in H-O-H bending as the temperature for annealing increases. For both the as-synthesized and the annealed samples, the absorption peak at about 1385 cm^{-1} indicates C- H stretching and after annealing, C-H stretching decreases. The peak at 2399 cm^{-1} for C1 confirms the presence of CH_2 vibration, revealing no presence of surfactant in the as-synthesized sample [7] and as the annealing temperature increases, the peak disappears indicating the reduction of CH_2 vibration. Typically, the peaks between 400 cm^{-1} and 600 cm^{-1} reveal Ce-O stretching [34-36]. For the C1, C2, C3, and C4 samples, the Ce-O stretching is seen at 576, 544, 471, and 535 cm^{-1}, respectively confirming the formation of CeO_2. As the annealing temperature increases, the peak due to Ce-O stretching becomes clearer and the high peak depth at 471cm^{-1} for C3 sample indicates the distinct formation of CeO_2 NPs in comparison to other annealed samples.

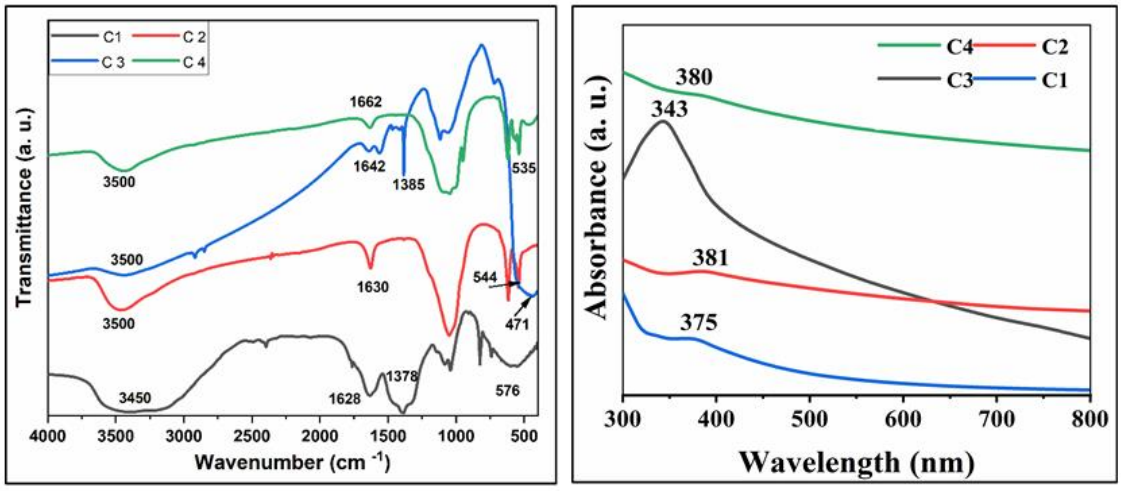

Figure 4.3: (a) FTIR spectroscopic images of samples C1, C2, C3 and C4 (b) UV-spectroscopic images of samples C1, C2, C3 and C4.

For further confirmation of CeO_2 NPs formations, UV-Vis analysis was performed within the wavelength range of 300–800 nm. The samples of CeO_2 NPs powder were first dispersed in DI water, and the suspensions were then used for UV-Vis analysis with a wavelength range of 300–800 nm. All of the sample's absorption peaks were observed between 343 and 375 nm (Fig. 4.3b). The higher peak at 343 nm in the C3 sample indicates more transfer of charge transitions that take place from O 2p to Ce 4f [36] in comparison to other samples due to the distinct presence of CeO_2 NPs (Fig. 4.3b).

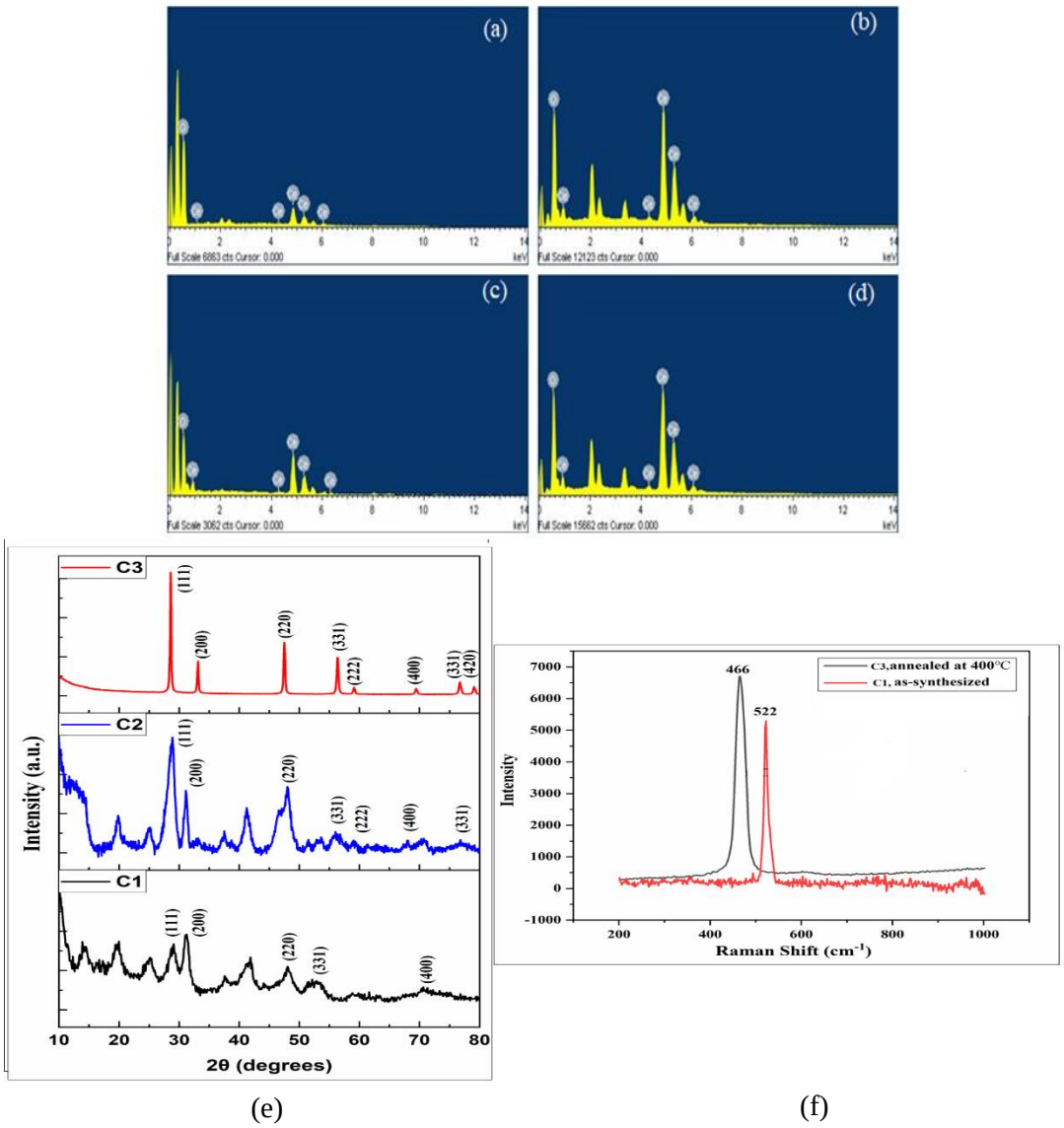

Figure 4.4. EDS spectra of the, samples (a) as-synthesized (C1), (b) C2 (c) C3 (d) C4 (e) XRD pattern of the as-synthesized CeO_2 NPs (C1) and annealed sample (C2, C3) (f) Raman spectra of C1 and sample C3.

The EDX spectra show the weight percentage of Ce as 34.18% and that of O as 65.82% in the case of C1 (Fig. 4.4a). The weight percentage of Ce increases with an increase in annealing temperature (Fig. 4.4b, Fig. 4.4c, and Fig.4.4d) indicating the decrease in H-O-H stretching as observed in FTIR analysis in Fig.4.3a. Based on FTIR and UV analysis of samples we have chosen the C3 sample (annealed at 400 °C) for further analysis along with the C1 sample (chosen for comparison purposes) due to more charge transfer from O to Ce.

The nanocrystallinity of prepared samples were characterized by XRD analysis (Fig. 4.4e). The XRD patterns of the C1, C2 samples show the lower intensity and broader

reflection due to the low crystalline formation of the NPs [37]. The spectrum exhibits some extra peaks associated with the impurities that may remain during the synthesis process. The well-defined and sharp peaks in the XRD spectra of annealed CeO_2 NPs (C3) centered at 2θ (28.05°), 2θ (33°), 2θ (47.5°), 2θ (56.39°), 2θ (59.19°), 2θ (69.42°) and 2θ (79.16°), correspond to the planes (111), (200), (220), (331), (222), (400), (JCPDS 043-1002). These planes depict the nanoceria's pure cubic fluorite structure [38]. The structure shows eight oxygen sites surrounding a cerium site in the FCC plane, with a tetrahedron cerium site on each oxygen site. It is evident from the spectra that upon annealing at 400 ℃, no impurity peaks appeared, confirming the successful synthesis of highly pure CeO_2 NPS. The crystal size (D) of the as-synthesized sample (C1) and the annealed sample (C3) were estimated by using the Scherrer formula, $D = [K\lambda/ (\beta\cos\theta)]$ where β is the line broadening at half the maximum intensity (FWHM), θ is the Bragg angle, and K= 0.89 (shape factor) and λ = 0.15406 nm and average crystal sizes (D) of C3 and C1 samples are obtained as 26.15 nm and 7.05 nm, respectively (Table 4.1). Different parameters (Diffraction angle, FWHM) extracted from the XRD spectrum are also presented in Table 4.1. The interfacial interaction leads to an increase in the crystal size as the calcination temperature rises [39]. The reflection peaks become sharper and narrower with a decrease in FWHM after annealing. This is because the crystal's activation energy decreases, which is associated with an improvement in CeO_2 nanocrystallite [7].

Table 4.1: Calculation of average crystal size of CeO_2 Nanoparticles particles

Sample	**FWHM,β (Degree)**	**2θ(Degree)**	**Crystal size(nm)**
As-synthesized	1.15	28.94	7.05
Annealed CeO_2 (at 400^0 C)	0.32819	47.515	26.15

For further confirmation of the formation of fluorite fcc structures, Raman spectra of C1 and C3 samples were carried out (Fig. 4.4f). The Raman spectrum for C1 reveals an active fundamental mode called triply degenerate F_{2g} mode at about 522.62 cm^{-1} indicating CeO_2's fluorite-type cubic crystal structure confirmed from the theoretical analysis [40]. This mode correlates to a symmetric Ce-O stretching vibration in the O_h point group representing the fluorite fcc structure's properties of oxygen atoms vibrating against one another. The reduction of thermal stability of the sample during annealing at

400 °C, leads to a minor shift towards a lower wavenumber in 466.73 cm^{-1} due to the electron-phonon interaction caused by the increase of particle size [41].

The Morphological analysis of C1 and C3 samples is performed by FESEM and

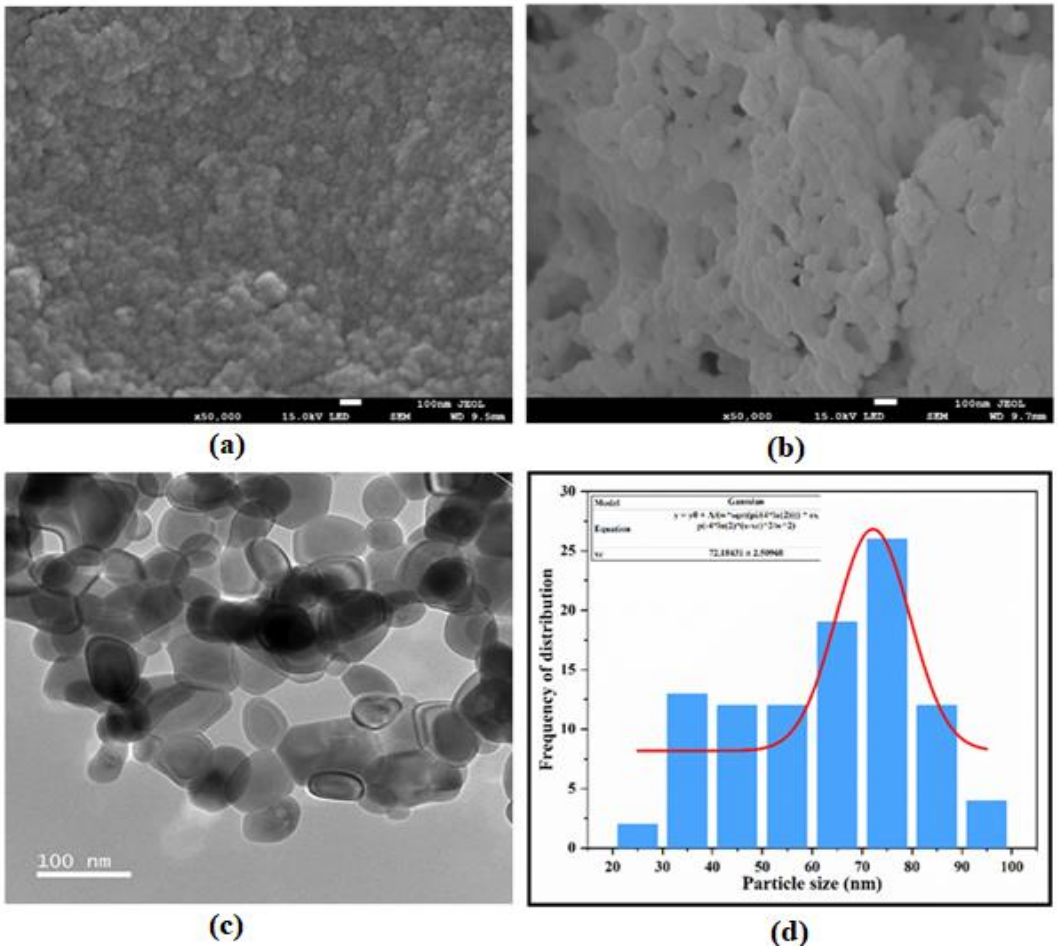

Figure 4.5: (a) FESEM image of the CeO_2 nanoparticles sample (C1) (b) FESEM image of the sample (C3) annealed at 400°C (c) TEM image of the sample (C3) at 100nm scale (d) Particle size histogram of annealed CeO_2 NPs (C3)

TEM imaging. The FESEM image of C1 in Fig. 4.5a shows the CeO_2 NPs uniformly distributed in nano-spherical forms over the surface. After annealing, the sample becomes less agglomerated (Fig. 4.5b) which is because the energy produced at high annealing temperatures makes nanoparticles depart from one another during calcination [42]. The TEM analysis is done for the C3 sample (Fig. 4.5c) showing the narrow size distribution of different shapes, ranging from spherical to polyhedral nano-particles with the presence of less agglomerated morphology. Using ImageJ software (open source), the size distribution histogram of 100 nanoparticles in the C3 sample was made showing the size of CeO_2 nanoparticles varied from 20 nm to 100 nm (Fig. 4.5d). The average size of nanoparticles is obtained as ~ 71 nm.

4.2.4 Preparation of $MgSiO_3.xH_2O$ –PVA composite

Here 500 mg of PVA powder was mixed with 10 ml of Deionized (DI) water. Then the mixture was vigorously stirred at 400 rpm for 3 h at 800 ℃ temperature until the PVA was completely dissolved. We have prepared different ratios of $MgSiO_3.xH_2O$+ PVA composite, to obtain 1 mM, 2 mM, and 4 mM solutions for deposition (Fig. 4.6a). $MgSiO_3.xH_2O$ powder and PVA were mixed by the aid of ultra-sonication and subsequently stirred at 400 rpm for 10 mins resulting in a homogeneous solution (Fig. 4.6a).

4.2.5 Characterization of $MgSiO_3.xH_2O$ –PVA composite

To investigate the surface functional groups of as-prepared samples FTIR analysis of $MgSiO_3.xH_2O$ and $MgSiO_3.xH_2O$ -PVA was performed using a spectrometer (NICOLET, IMPACT 410 OMNIC E.S.P.5.0) in the range of 400- 4000 cm^{-1} and

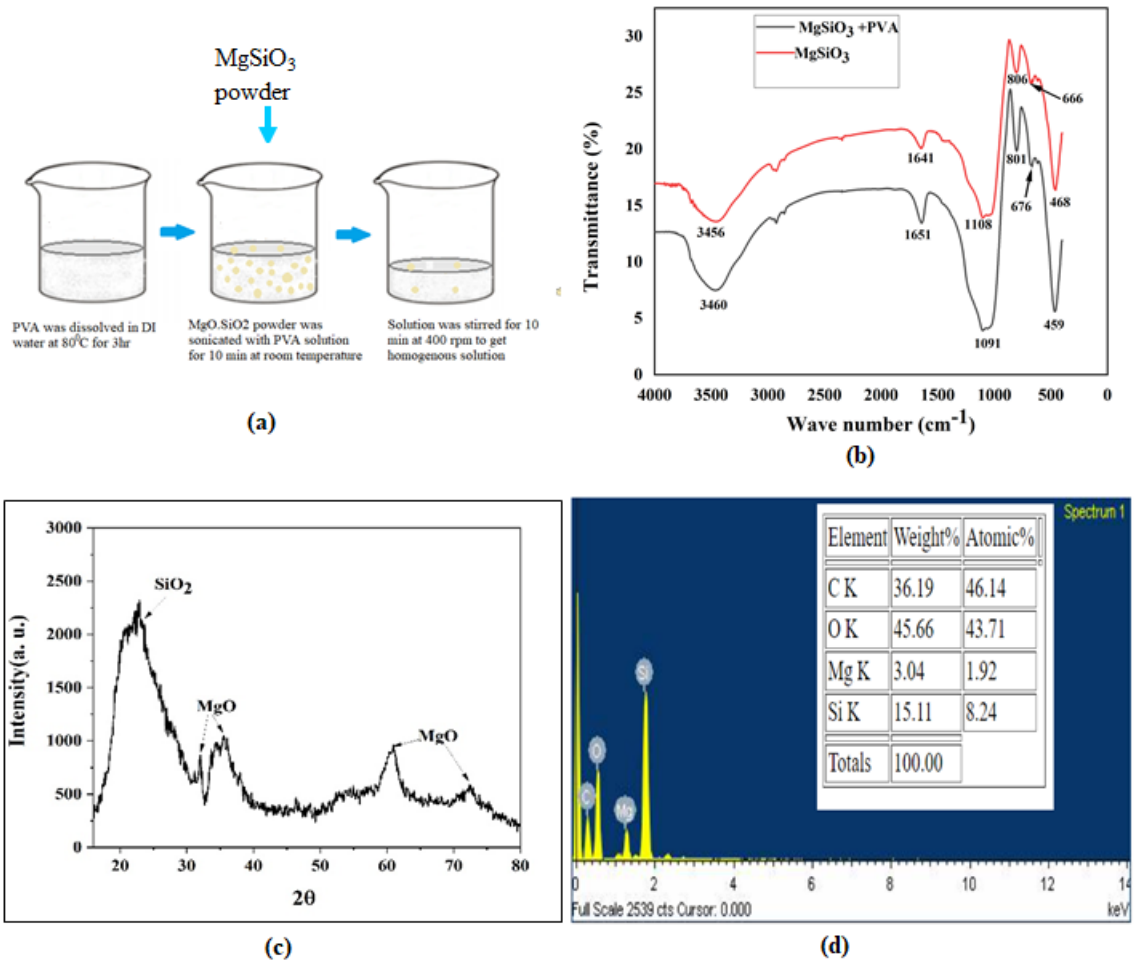

Figure 4.6: (a) the process showing the synthesis of magnesium silicate and PVA composite (b) FTIR analysis of $MgSiO_3.xH_2O$ and $MgSiO_3.xH_2O$ + PVA (c) XRD pattern of Magnesium silicate ($MgSiO_3.xH_2O$) (d) EDX analysis showing weight and atomic percentage of the composite

recorded in Fig. 4.6b. Powder X-ray diffraction (PXRD) pattern was carried using BRUKER, D8 Focus diffractometer as shown in Fig. 4.6c. Surface morphology was studied using scanning electron spectroscopy (SEM, JEOL, JSM 6390LV) and Energy Dispersive X-Ray Analysis (EDX) was also carried out to identify the elemental composition of materials. EDX and SEM images are shown in Fig. 4.6d and Fig. 4.7 respectively.

The Fourier transform infrared (FTIR) spectrum of magnesium silicate and magnesium silicate / PVA composite are shown in Fig. 4.6b. The broadband between 3200 cm^{-1} and 3700 cm^{-1} in both figures shows the fundamental stretching of hydroxyl groups (O–H) [32]. The small peaks at 1641 cm^{-1} and 1651 cm^{-1} indicate water absorption in Magnesium silicate ($MgSiO_3.xH_2O$) and $MgSiO_3.xH_2O$ - PVA composite respectively [43]. The vibration band at 1108 cm^{-1} (Fig. 4.6b) indicates the symmetrical stretching vibration of Si–O–Si of Magnesium silicate. The vibration bands at 1091 cm^{-1} (Fig. 4.6b) indicating stretching of C-O and bending of OH (amorphous sequence of PVA), confirms the presence of PVA in magnesium silicate / PVA composite [43]. In addition, the peaks that occurred at 468 cm^{-1} and 459 cm^{-1} as shown in Fig. 4.6b reveal Si− O bending vibrations of the MgO [44]. The small peak at 2927 cm^{-1} showing C−H stretching confirms the presence of PVA in $MgSiO_3.xH_2O$ - PVA composite [43]. The band at 666 cm^{-1} (Fig. 4.6b) is due to a Si–O bending motion for magnesium silicate [44] and the same bending is observed at 676 cm^{-1} for $MgSiO_3.xH_2O$- PVA composite.

The powder XRD pattern of magnesium silicate is shown in Fig. 4.6c. All over the diffraction pattern, Magnesium silicate shows broad peaks indicating the non-crystalline structure of the particles. The broadband centered at 2θ (33.08°), 2θ (60.55°) and 2θ (72.26°) corresponds to the planes (111), (202) and (113) respectively matching with MgO (JCPDS No. 78-0430) [45]. The broadband peak centered at 2θ = 22.58° matches with the characteristic peak for amorphous SiO_2 corresponding to the (003) plane (JCPDS No. 29-0085) [45]. Using Scherrer equation $D = [K\lambda/ (\beta\cos\theta)]$ and taking the value K= 0.89 and λ =0.15406 nm, the average crystal size (D) of the prepared sample was calculated to be 2.12 nm (Table 4.2) [41].

The notable peaks of O as shown in Fig. 4.6d of EDX spectra indicate the possible formation of O-H bonding as supported by the FTIR result. The carbon to oxygen weight % ratio that depends upon the composite ratio of $MgSiO_3.xH_2O$ and PVA is found to be

Table 4.2: Calculation of average crystal size of MgSiO3 particles

FWHM (Degree)	2θ(Degree)	Miller indices	Crystal size(nm)	Average crystal size(nm)
3.71	60.55	202	2.45193	2.121022
2.323	72.26	113	4.1871	
12.07	33.08	111	0.678966	
6.87	22.58	003	1.166091	

0.79. The weight percentage of Mg, Si, O and C were found to be 3.04%, 15.11%, 45.66%, and 36.19% respectively.

The SEM image (Fig. 4.7) shows discontinuous precipitation of $MgSiO_3.xH_2O$ and PVA composite due to having formation of agglomeration structure. In the figure,

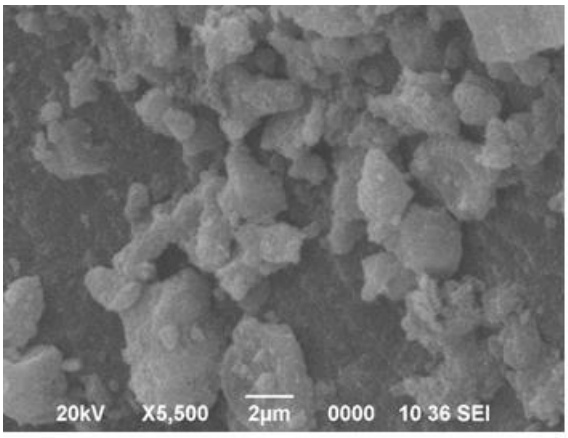

Figure 4.7: SEM image of $MgSiO_3.xH_2O$ and PVA composite

there are large and secondary agglomerates with sizes varying from 1 μm to 4 μm observed on SEM images indicating $MgSiO_3.xH_2O$-PVA composites [46]. Very less sharp nano edges of size below 500 nm are observed for the collected particles indicating PVA in composite samples [47]

4.3 Sensor fabrication

Fig 2a in chapter 2 shows the capacitor sensor based on interdigitated electrodes made on a flexible paper substrate. The geometrical structure in Fig 2b of chapter 2 reveals the planner electrodes with eight numbers of fingers making the interdigitated pattern of the capacitive sensor. Here "W_f" and "G" stand for the electrode finger's width and the gap between the fingers, respectively. The L_f, W_e and L_e represent the overlapping length of electrode fingers, the width of the electrode and the length of the electrode respectively. The ratio $G/(G+ W_f)$ represents the metallization ratio (η).

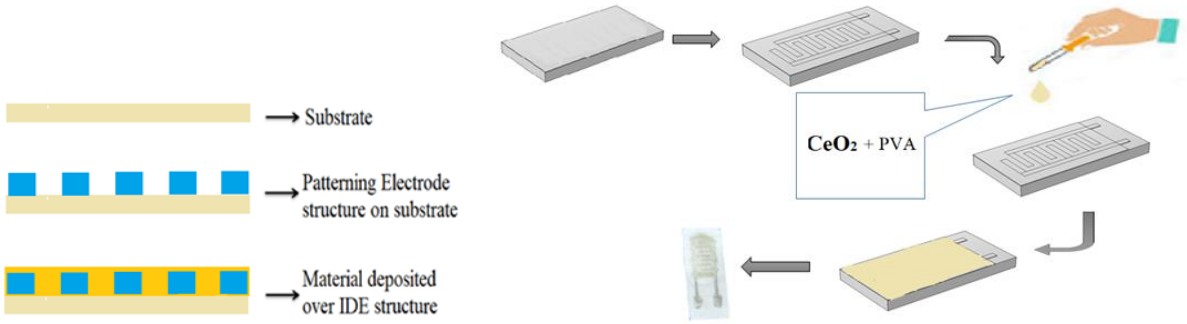

(a) (b)

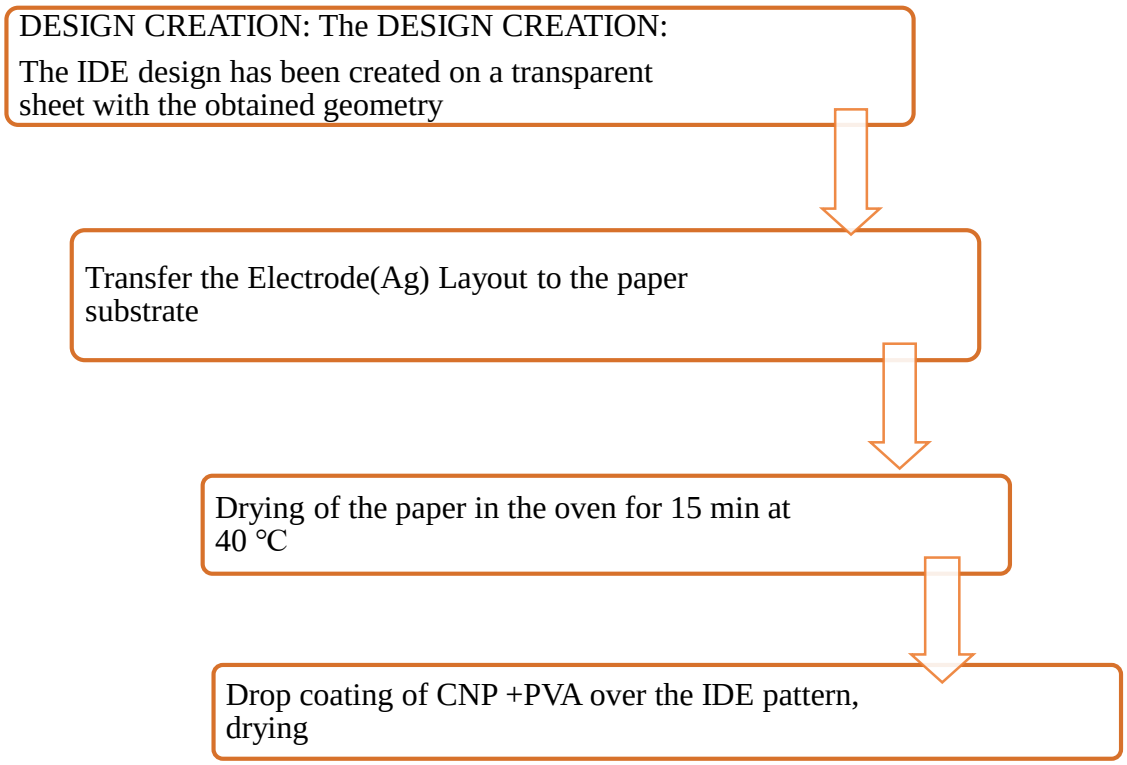

(c)

Figure 4.8: (a) Showing fabrication steps and (b) drop coating of CeO_2 +PVA over the IDE device (c) Fabrication flow chart of IDE sensor

For making the IDE sensor, we have used the 6 mm × 8 mm whatman 1 filter paper which is biodegradable, flexible and environmentally friendly [48-52]. The interdigitated electrode fingers structure having W_f =1, W_e =1 mm and G = 1 mm was made on the

substrate with the silver paste using the screen printing technique as per the design (Fig.4.8a and 4.8b). The overlapping length for the electrodes was kept to be ~ 5 mm. Fig 4.8c shows the details of flow chart of fabrication of IDE sensors using CeO_2 NPs as sensing layer. First the IDE pattern of the dimension as obtained was made on a transparent sheet. Then with the help of the pattern and by employing the methodology of screen printing, the Ag material is deposited on the surface of cellulose paper. The paper is dried at 40 ℃ for approximately 10- 15 mins and get ready to use for deposition. The CeO_2 NPs (powder) of 10 mg was mixed with 1 ml of PVA solution to prepare $Ce0_2$ NPs and PVA composite to form gel for the drop coating on the paper substrate. After the deposition of approximately 20µL (weighing ≈2mg) volume of gel of CeO_2 NPs and PVA composite by drop coating over the IDE patterned paper substrate, the fabricated sensor was dried at 40^0 C for 20 mins to make it ready for analysis. Similarly, $MgSiO_3.xH_2O$ -PVA composite of different wt% such as 2 wt%, 4 wt% and 6 wt% were deposited over the electrode surface with same procedure and quantity as followed for CeO_2 NPs based sensor. The thickness of the film was not experimentally measured, but from the parameters such as volume and particle size of materials composite, wt % of the composite, the thickness of the film was assumed to be within 1 to 5µm[53]. The wires were bonded at the electrodes and crocodile clips were used at the two ends to connect the sensor's output to the embedded circuit for processing the sensing signal.

4.4 Sensor's output measurement set-up

Recently, the gas and humidity sensor based on expensive Au/Ti comb finger structure over Si substrate are reported but its sensing measurement uses a bulky impedance analyzer causing difficulty for onsite measurement [54, 55]. In the course of making the sensor simple, flexible and cost-effective, we have used Whatman 1 filter paper which is biodegradable, flexible and environmentally friendly [48]. In overcoming the limitation of using an impedance analyzer for onsite measurement, a simple and portable set-up (Fig. 4.9a) for

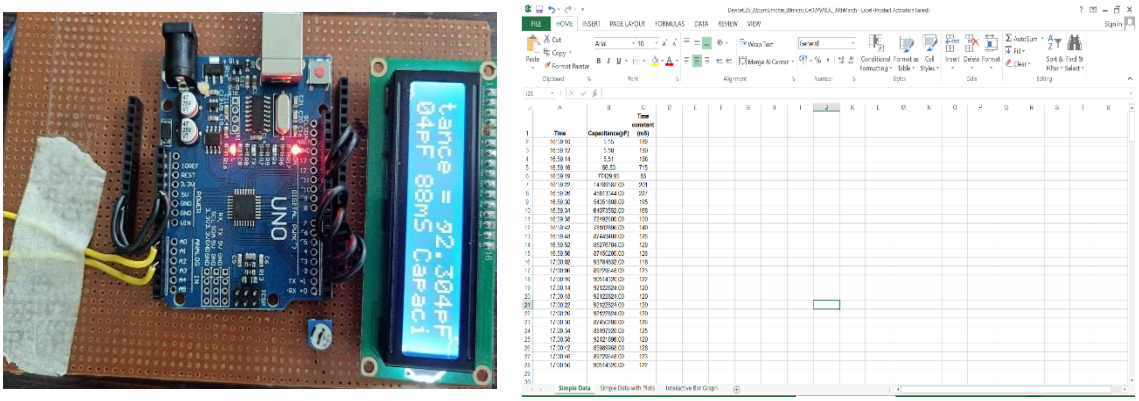

(a) (b)

Figure 4.9: a) The capacitance measuring set-using Arduino UNO b) the PLX-DAQ data acquisition in PC

onsite monitoring has been developed where, the sensor's output signal was fed to the microcontroller's (ATmega32) analog pin embedded in the Arduino UNO which changes its response following the property of the sensing material. The sensor's output was serial monitored and stored as shown Fig. 4.9b in the personal computer (PC) through the open source software PLX-DAQ. The IDE sensor's response in terms of capacitance was estimated from the equation

$$C=(-t/R)(1/\log(1-(q/VC)) \qquad (4.1)$$

Here, V is the applied voltage. At a time when q=VC, C=τ/R, τ is called the time constant equal to RC where, R is the in-build series resistance through which the capacitor gets charged, C is unknown capacitor. The Time Constant (τ) is defined as the time taken to charge a capacitor (C) through a resistor (R) to reach 63.2 % of the maximum supply voltage. The measuring set-up was calibrated with the standard capacitors with ranges varying from 47 pF to 470 µF. Fig. 4.10 shows the schematic of whole set up that includes all the measuring components.

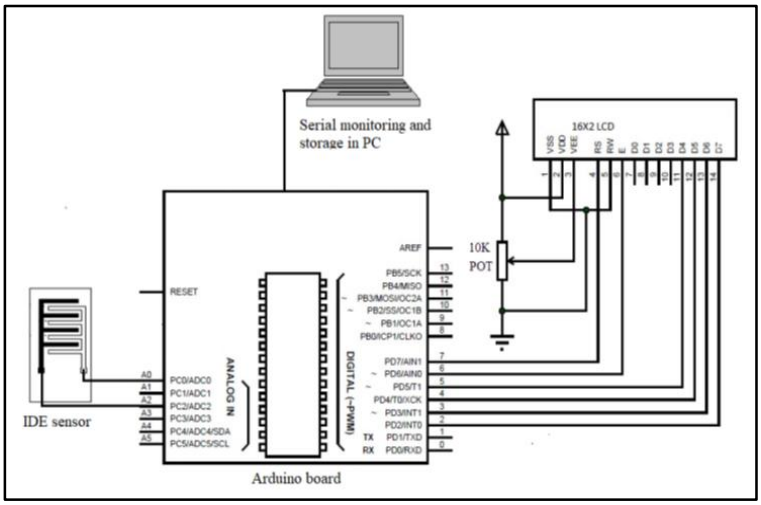

Figure 4.10: Sensing setup

The accuracy of the measurement in terms of the percentage error is within ±6% (Table 4.3). The sensor was calibrated for different limonin concentrations at room temperature, ranging from 1 ppm to 20 ppm. The sensor's performance was analyzed by studying its accuracy, specificity, sensitivity, shelf-life, reusability and response time. Due to the interaction of CeO_2 NPs with limonin affecting the capacitance of the fabricated sensor, an attempt has been made to measure the concentration of limonin.

Table4.3: Accuracy measurement of the capacitance measuring set up

Actual capacitance (standard)	Measured capacitance by the measuring unit	Accuracy(in terms of % error)	Average Accuracy(in terms of % error)
47 pF	47.32 pF	-0.6667	± 6.33%
1 nF	1.17 nF	-17	
10 nF	10.28 nF	-2.8	
1 µF	0.95783 µF	4.217	
4.7 µF	4.66 µF	0.851	
10 µF	10.23 µF	-2.3	
100µF	102.02 µF	-2.02	
220 µF	243.83 µF	-13.5591	
470 µF	534 µF	-13.617	

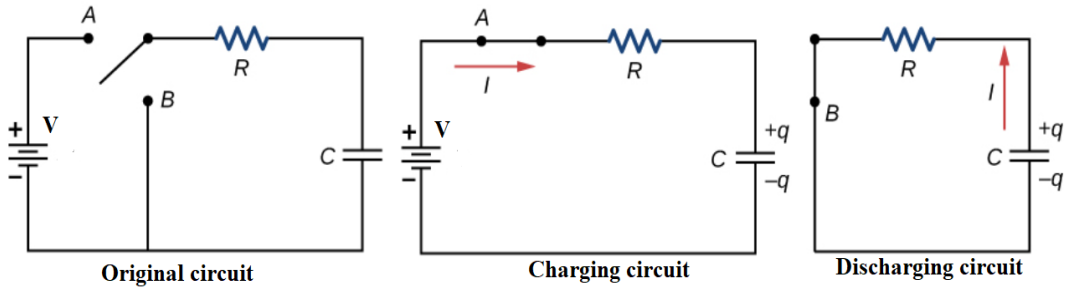

(a)

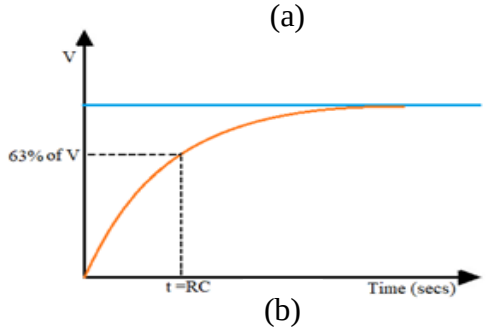

(b)

Figure 4.11: (a) The equivalent circuit, showing charging and discharging of capacitor, Here, V- Supplied voltage, C=Cap. R= resistor through which the capacitor gets charged (b) the charging curve for capacitor

Fig 4.11a shows a RC circuit with a two-pole switch that can be used to charge and discharge a capacitor. When the switch is moved to position A, the circuit reduces to a simple series connection of the voltage source, the resistor, the capacitor, and the switch.

When the switch is moved to position B, the circuit reduces to a simple series connection of the resistor, the capacitor, and the switch and the voltage source is removed from the circuit. We have used this concept of charging and discharging of our IDE sensor for its capacitance measurement which is finally used for predicting the analyte concentration in juice sample. The Kirchhoff's loop rule was used to understand the charging of the capacitor. This results in the equation $V-V_R-V_C=0$. This equation can be used to model the charge as a function of time as the capacitor charges. Capacitance is defined as $C=q/V$, so the voltage across the capacitor is $V_C=q/C$. Using Ohm's law, the potential drop across the resistor is $V_R=IR$, and the current is defined as $I=dq/dt$,

$$V-V_R-V_C=0$$

$$V-IR-q/C=0,$$

$$V-Rdq/dt-q/C=0$$

This differential equation can be integrated to find an equation for the charge on the capacitor as a function of time.

$$V-Rdq/dt-q/C=0$$

$$dq/dt=(VC-q)/RC$$

$$\int(1/(VC-q))dq=1/RC\int dt, \text{ integration from 0 to t}$$

Simplifying results in an equation of the capacitance for the charging capacitor as a function of time we have the equation for capacitance as,

$$C=(-t/R)(1/\log(1-(q/VC))$$

$$\text{Or } V_c=V_s\,(1-c^{t/RC})$$

Here, V_s is the voltage at t= RC. A graph of the charge on the capacitor versus time is shown in Fig. 4.11b. The exponential decreases to zero as the time approaches infinity, bringing the charge closer to the maximum charge Q=CV, which is measured in coulombs. Secondly, the units of time, are the units of RC. The time constant is represented by the expression =RC. The charge equals $1-e^{-1}=1-0.368=0.632$ of the maximal charge Q=CV at time t==RC. As time goes on, the slope of the graph decreases until it eventually reaches zero. The current through the resistor reduces as the capacitor's charge increases. The circuit reduces to the circuit as shown in Fig. 4.11a when switched to position B, allowing the charged capacitor to discharge through the resistor. Hence this concept of charging as well as discharging the sensor as capacitor was used for measurement of limonin concentration in terms of capacitance measurement. The

calibration, detection and performance of CeO_2 NPs made IDE sensor is discussed in chapter 5.

4.5 Summary

CeO_2 NPs were successfully synthesized for the first time with the use of the aqueous extract of D. indica by means of a green synthesis approach. The peaks obtained for UV spectra are in the range from 400 cm^{-1} to 600 cm^{-1} for the synthesized NPs samples annealed at a different temperature which are assigned to Ce−O stretching. The crystal size for as-synthesized and annealed (400 °C) NPs have been found to as 7.05 nm and 26.15 nm respectively which shows an increase in crystallite size of polycrystalline cerium nanoparticles with fcc structure with an increase in annealed temperature. Here, D. indica-mediated green synthesized NPs have lower crystallite size compared to the NPs synthesized by Acalypha indica leaf extract and by pectin at the same calcination temperature. The morphology of the particles changed into a spherical shape of approximately 70 nm of average size as calculated from FESEM images which is higher than the crystal size as calculated from XRD analysis. The magnesium silicate / PVA composite material has been successfully prepared and characterized. The FTIR spectrum of magnesium silicate and magnesium silicate / PVA composite shows the vibration band at 1108 cm^{-1} indicating the symmetrical stretching vibration of Si–O–Si of Magnesium silicate. The vibration bands at 1091 cm^{-1} indicating stretching of C-O and bending of OH (amorphous sequence of PVA), confirm the presence of PVA in magnesium silicate / PVA composite. The XRD pattern of magnesium silicate shows broad peaks indicating the non-crystalline structure of the particles. The average crystal size (D) of the prepared sample was calculated to be 2.12 nm. The fabrication process of the sensor exhibits simple, flexible, low-cost features. The measuring circuit based on a microcontroller unit is portable one and has been developed with the features of storing continuous data in the computer. The measuring setup was analysed for its accuracy and a deviation of ±6% was observed for the measurement set-up while calculating its accuracy. In the succeeding chapter 5, the fabricated device based on CeO_2 will be used for assessment of limonin in citrus fruit juices.

Bibliography

[1] Korsvik, C., Patil, S., Seal, S. and Self, W. T. Superoxide dismutase mimetic properties exhibited by vacancy engineered ceria nanoparticles. *Chemical communications*, (10):1056-1058, 2007.

[2] Singh, K. R., Nayak, V., Sarkar, T. and Singh, R. P. Cerium oxide nanoparticles: properties, biosynthesis and biomedical application. *RSC advances*, 10(45):27194-27214, 2020.

[3] Rico, C. M. and Majumdar, S. J. l. Gardea-Toressdey. *J. Agr. Food Chem*, 59(8):3485-3498, 2011.

[4] Fard, J. K., Jafari, S. and Eghbal, M. A. A review of molecular mechanisms involved in toxicity of nanoparticles. *Advanced pharmaceutical bulletin*, 5(4):447, 2015.

[5] Trovarelli, A. Catalytic properties of ceria and CeO2-containing materials. *Catalysis Reviews*, 38(4):439-520, 1996.

[6] Wang, C.-H. and Lin, S.-S. Preparing an active cerium oxide catalyst for the catalytic incineration of aromatic hydrocarbons. *Applied Catalysis A: General*, 268(1-2):227-233, 2004.

[7] Arumugam, A., Karthikeyan, C., Hameed, A. S. H., Gopinath, K., Gowri, S. and Karthika, V. Synthesis of cerium oxide nanoparticles using Gloriosa superba L. leaf extract and their structural, optical and antibacterial properties. *Materials Science and Engineering: C*, 49:408-415, 2015.

[8] Das, S., Dowding, J. M., Klump, K. E., McGinnis, J. F., Self, W. and Seal, S. Cerium oxide nanoparticles: applications and prospects in nanomedicine. *Nanomedicine*, 8(9):1483-1508, 2013.

[9] Liying, H., Yumin, S., Lanhong, J. and Shikao, S. Recent advances of cerium oxide nanoparticles in synthesis, luminescence and biomedical studies: a review. *Journal of rare earths*, 33(8):791-799, 2015.

[10] George, S., Pokhrel, S., Xia, T., Gilbert, B., Ji, Z., Schowalter, M., Rosenauer, A., Damoiseaux, R., Bradley, K. A. and Mädler, L. Use of a rapid cytotoxicity screening approach to engineer a safer zinc oxide nanoparticle through iron doping. *ACS nano*, 4(1):15-29, 2010.

[11] Mishra, S. R. and Ahmaruzzaman, M. Cerium oxide and its nanocomposites: Structure, synthesis, and wastewater treatment applications. *Materials Today Communications,* 28:102562, 2021.

[12] Kannan, S. and Sundrarajan, M. A green approach for the synthesis of a cerium oxide nanoparticle: characterization and antibacterial activity. *International journal of nanoscience,* 13(03):1450018, 2014.

[13] Soren, S., Jena, S. R., Samanta, L. and Parhi, P. Antioxidant potential and toxicity study of the cerium oxide nanoparticles synthesized by microwave-mediated synthesis. *Applied biochemistry and biotechnology,* 177(1):148-161, 2015.

[14] Lee, S. S., Song, W., Cho, M., Puppala, H. L., Nguyen, P., Zhu, H., Segatori, L. and Colvin, V. L. Antioxidant properties of cerium oxide nanocrystals as a function of nanocrystal diameter and surface coating. *ACS nano,* 7(11):9693-9703, 2013.

[15] Hayes, B. L. Recent advances in microwave-assisted synthesis. *Aldrichimica Acta,* 37(2):66-77, 2004.

[16] Lee, J.-S. and Choi, S.-C. Crystallization behavior of nano-ceria powders by hydrothermal synthesis using a mixture of H2O2 and NH4OH. *Materials Letters,* 58(3-4):390-393, 2004.

[17] Oh, H. and Kim, S. Synthesis of ceria nanoparticles by flame electrospray pyrolysis. *Journal of Aerosol Science,* 38(12):1185-1196, 2007.

[18] Yin, L., Wang, Y., Pang, G., Koltypin, Y. and Gedanken, A. Sonochemical synthesis of cerium oxide nanoparticles—effect of additives and quantum size effect. *Journal of Colloid and Interface Science,* 246(1):78-84, 2002.

[19] Terribile, D., Trovarelli, A., Llorca, J., de Leitenburg, C. and Dolcetti, G. The synthesis and characterization of mesoporous high-surface area ceria prepared using a hybrid organic/inorganic route. *Journal of Catalysis,* 178(1):299-308, 1998.

[20] Nadeem, M., Tungmunnithum, D., Hano, C., Abbasi, B. H., Hashmi, S. S., Ahmad, W. and Zahir, A. The current trends in the green syntheses of titanium oxide nanoparticles and their applications. *Green Chemistry Letters and Reviews,* 11(4):492-502, 2018.

[21] Srikar, S., Giri, D., Pal, D., Mishra, P. and Upadhyay, S. Green synthesis of silver nanoparticles: a review, Green Sustain. Chem. 6 (2016) 34–56. 2016.

[22] Kulkarni, N. and Muddapur, U. Biosynthesis of metal nanoparticles: a review. *Journal of Nanotechnology,* 2014, 2014.

[23] Xiao, Z., Yuan, M., Yang, B., Liu, Z., Huang, J. and Sun, D. Plant-mediated synthesis of highly active iron nanoparticles for Cr (VI) removal: investigation of the leading biomolecules. *Chemosphere,* 150:357-364, 2016.

[24] Milani, N., McLaughlin, M. J., Stacey, S. P., Kirby, J. K., Hettiarachchi, G. M., Beak, D. G. and Cornelis, G. Dissolution kinetics of macronutrient fertilizers coated with manufactured zinc oxide nanoparticles. *Journal of agricultural and food chemistry*, 60(16):3991-3998, 2012.

[25] Giraldo, J. P., Landry, M. P., Faltermeier, S. M., McNicholas, T. P., Iverson, N. M., Boghossian, A. A., Reuel, N. F., Hilmer, A. J., Sen, F. and Brew, J. A. Plant nanobionics approach to augment photosynthesis and biochemical sensing. *Nature materials*, 13(4):400-408, 2014.

[26] Korotkova, A. M., Borisovna, P. O., Aleksandrovna, G. I., Bagdasarovna, K. D., Vladimirovich, B. D., Vladimirovich, K. D., Alexandrovich, F. A., Yurievna, K. M., Nikolaevna, B. E. and Aleksandrovich, K. D. " Green" Synthesis of Cerium Oxide Particles in Water Extracts Petroselinum crispum. *Current Nanomaterials,* 4(3):176-190, 2019.

[27] Khan, S. A. and Ahmad, A. Fungus mediated synthesis of biomedically important cerium oxide nanoparticles. *Materials Research Bulletin*, 48(10):4134-4138, 2013.

[28] Darroudi, M., Hoseini, S. J., Oskuee, R. K., Hosseini, H. A., Gholami, L. and Gerayli, S. Food-directed synthesis of cerium oxide nanoparticles and their neurotoxicity effects. *Ceramics International*, 40(5):7425-7430, 2014.

[29] Sett, A., Gadewar, M., Sharma, P., Deka, M. and Bora, U. Green synthesis of gold nanoparticles using aqueous extract of Dillenia indica. *Advances in Natural Sciences: Nanoscience and Nanotechnology,* 7(2):025005, 2016.

[30] Barmore, C. R., Fisher, J. F., FELLERS, P. J. and Rouseff, R. L. Reduction of bitterness and tartness in grapefruit juice with Florisil. *Journal of Food Science*, 51(2):415-416, 1986.

[31] Puri, M., Marwaha, S., Kothari, R. and Kennedy, J. Biochemical basis of bitterness in citrus fruit juices and biotech approaches for debittering. *Critical reviews in biotechnology,* 16(2):145-155, 1996.

[32] Panicker, N. J. and Sahu, P. P. Green reduction of graphene oxide using phytochemicals extracted from Pomelo Grandis and Tamarindus indica and its supercapacitor applications. *Journal of Materials Science: Materials in Electronics*:1-14, 2021.

[33] Das, S. and Sahu, P. P. A novel electrochemical interdigitated electrodes sensor for limonin quantification and reduction in citrus limetta juice. *Food Chemistry*:132248, 2022.

[34] Reinhardt, K. and Winkler, H. Cerium mischmetal, cerium alloys, and cerium compounds. *Ullmann's encyclopedia of industrial chemistry*, 2000.

[35] Liu, Y., Zuo, J., Ren, X. and Yong, L. Synthesis and character of cerium oxide (CeO 2) nanoparticles by the precipitation method. *Metalurgija,* 53(4):463-465, 2014.

[36] Farahmandjou, M. and Zarinkamar, M. Synthesis of nano-sized ceria (CeO2) particles via a cerium hydroxy carbonate precursor and the effect of reaction temperature on particle morphology. *Journal of Ultrafine Grained and Nanostructured Materials*, 48(1):5-10, 2015.

[37] Singh, A. K. Advanced x-ray techniques in research and industry. 2005, IOS press.

[38] Darroudi, M., Sarani, M., Oskuee, R. K., Zak, A. K., Hosseini, H. A. and Gholami, L. Green synthesis and evaluation of metabolic activity of starch mediated nanoceria. *Ceramics International*, 40(1):2041-2045, 2014.

[39] Yang, H., Huang, C., Tang, A., Zhang, X. and Yang, W. Microwave-assisted synthesis of ceria nanoparticles. *Materials research bulletin*, 40(10):1690-1695, 2005.

[40] Shyu, J., Weber, W. and Gandhi, H. Surface characterization of alumina-supported ceria. *The Journal of Physical Chemistry*, 92(17):4964-4970, 1988.

[41] Narzary, R., Phukan, P. and Sahu, P. P. Efficiency Enhancement of Low-Cost Heterojunction Solar Cell by the Incorporation of Highly Conducting rGO Into ZnO Nanostructure. *IEEE Transactions on Electron Devices*, 2021.

[42] Sangsefidi, F. S., Salavati-Niasari, M., Mazaheri, S. and Sabet, M. Controlled green synthesis and characterization of CeO2 nanostructures as materials for the determination of ascorbic acid. *Journal of Molecular Liquids*, 241:772-781, 2017.

[43] Jipa, I. M., Stoica, A., Stroescu, M., Dobre, L.-M., Dobre, T., Jinga, S. and Tardei, C. Potassium sorbate release from poly (vinyl alcohol)-bacterial cellulose films. *Chemical Papers*, 66(2):138-143, 2012.

[44] Rashid, I., Daraghmeh, N. H., Al Omari, M. M., Chowdhry, B. Z., Leharne, S. A., Hodali, H. A. and Badwan, A. A. Magnesium silicate. in Profiles of drug substances, excipients and related methodology. 2011, Elsevier. p. 241-285.

[45] Zhang, T., Vandeperre, L. J. and Cheeseman, C. R. Formation of magnesium silicate hydrate (MSH) cement pastes using sodium hexametaphosphate. *Cement and Concrete Research*, 65:8-14, 2014.

[46] Sun, Z., Duan, X., Srinivasakannan, C. and Liang, J. Preparation of magnesium silicate/carbon composite for adsorption of rhodamine B. *RSC advances*, 8(14):7873-7882, 2018.

[47] Riyadh, S. M., Khalil, K. D. and Bashal, A. H. Structural properties and catalytic activity of binary poly (vinyl alcohol)/Al2O3 nanocomposite film for synthesis of thiazoles. *Catalysts*, 10(1):100, 2020.

[48] Singh, A. T., Lantigua, D., Meka, A., Taing, S., Pandher, M. and Camci-Unal, G. based sensors: Emerging themes and applications. *Sensors*, 18(9):2838, 2018.

[49] Gaspar, C., Olkkonen, J., Passoja, S. and Smolander, M. Paper as active layer in inkjet-printed capacitive humidity sensors. *Sensors*, 17(7):1464, 2017.

[50] Martinez, A. W., Phillips, S. T., Whitesides, G. M. and Carrilho, E. Diagnostics for the developing world: microfluidic paper-based analytical devices. 2010, ACS Publications.

[51] Ellerbee, A. K., Phillips, S. T., Siegel, A. C., Mirica, K. A., Martinez, A. W., Striehl, P., Jain, N., Prentiss, M. and Whitesides, G. M. Quantifying colorimetric assays in paper-based microfluidic devices by measuring the transmission of light through paper. *Analytical Chemistry*, 81(20):8447-8452, 2009.

[52] Gao, B., Chi, J., Liu, H. and Gu, Z. Vertical paper analytical devices fabricated using the principles of quilling and kirigami. *Scientific reports*, 7(1):1-8, 2017.

[53] Hemalatha, K. and Rukmani, K. Poly vinyl alcohol-CeO2 nanocomposite films: a promising material for NO2 sensors at high temperatures. *Materials Research Express*, 6(8):085008, 2019.

[54] Leng, X., Wang, Y. and Wang, F. Humidity Sensing: Alcohols Assisted Hydrothermal Synthesis of Defect-Rich MoS2 and Their Applications in Humidity Sensing (Adv. Mater. Interfaces 11/2019). *Advanced Materials Interfaces*, 6(11):1970068, 2019.

[55] Veerappan, M., Leng, X., Luo, D. and Wang, F. Dandelion flower like GaN humidity sensor: Fabrication and its excellent linearity towards entire relative humidity range. *IEEE Sensors Journal*, 21(3):2581-2588, 2020.